Pedestrian dynamics at the running of the bulls evidences an inaccessible region in the fundamental diagram

Daniel R.Parisi[a,1], **Alan G. Sartorio**[b], **Joaquín R. Colonnello**[b], **Angel Garcimartín**[c], **Luis A. Pugnaloni**[d], **and Iker Zuriguel**[c]

[a]Instituto Tecnológico de Buenos Aires (ITBA), CONICET, Lavardén 315, (1437) C.A.B.A, Argentina; [b]Instituto Tecnológico de Buenos Aires (ITBA), Av. E. Madero 399, (1106) C.A.B.A, Argentina; [c]Departamento de Física y Mat. Apl., Facultad de Ciencias, Universidad de Navarra, E-31080 Pamplona, Spain; [d]Departamento de Física, FCEyN, Universidad Nacional de La Pampa, CONICET, Uruguay 151, (6300) Santa Rosa, Argentina

We characterize the dynamics of runners in the famous "Running of the Bulls" festival by computing the individual and global velocities and densities, as well as the crowd pressure. In contrast with all previously studied pedestrian systems, we unveil a unique regime in which speed increases with density, that can be understood in terms of a time-dependent desired velocity of the runners. Also, we discover the existence of an inaccessible region in the speed-density state diagram that is explained by falls of runners. With all these ingredients, we propose a generalization of the pedestrian fundamental diagram for a scenario in which people with different desired speeds coexist.

Pedestrian Dynamics | Fleeing Behavior | Fundamental Diagram | High-Speed Pedestrians

The world-famous Running of the Bulls (San Fermín) Festival constitutes a unique system of pedestrians running away from bulls at the streets of Pamplona (Spain). Curiously, despite this race has been repeatedly used as an illustration of competitive pedestrian dynamics, it has not been studied in detail until now. Runners, first waiting for and then escaping from bulls, constitute a fascinating annual scenario of real fleeing pedestrians, becoming an invaluable opportunity for studying and understanding extreme pedestrian dynamics.

One of the main macroscopic observables for characterizing pedestrian systems is the fundamental diagram derived from the speed-density relation for a group of moving pedestrians (1–16). This relation, which is used as a benchmark in design and planning (17–20), accounts for the accepted fact that the speed of the group decreases monotonically as the density increases. Under ordinary conditions, this behavior can be explained because people try to avoid physical contact and slow down when the available space reduces. A key feature of this plot is the speed at near-zero density, which indicates the velocity at which pedestrians would move if they were alone. This speed is known as the desired speed or the free speed (v_0).

Given their importance, speed-density relations are widely studied in the literature; however, most of the existing investigations assume implicitly two essential facts:

- All pedestrians have constant desired speed normally distributed with small variance (an exception to this is the time dependent desired speed implemented in (21)).
- The speed-density relations correspond to stationary (or quasi-stationary) pedestrian systems.

Importantly, these premises hold even for the fundamental diagrams obtained in extreme conditions. As examples, we highlight the fundamental diagram for running pedestrians at medium speed (16); the empirical results collected in a real event (8); and the outcomes obtained in highly competitive evacuation drills in which pedestrians were allowed to push each other (22). In these last two cases, very high densities were present (which dominate the dynamics) and the free velocities were below 1.5 m/s. Remarkably, the assumptions used for traditional fundamental diagrams are not valid in the Running of the Bulls festival. Here, a moving threat (the bulls) induces time-dependent desired velocities along with a broad distribution among individuals. In order to understand the complicated dynamics observed, we characterize this system by studying -among other variables- the speed, density, and falling probability of the pedestrians.

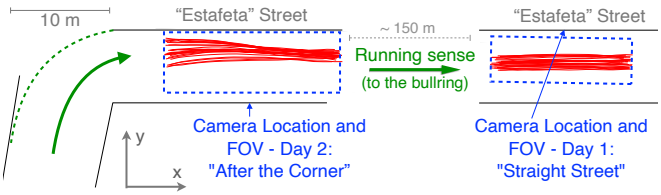

Fig. 1. Layout of the street and locations where the videos were recorded on July 8 (Day 1) and July 9 (Day 2). Dotted rectangles indicate the field of view (FOV) of the camera. Blue arrows indicate the camera position. Red lines show recorded bull trajectories (heads and tails).

The pedestrian system

During the week of the San Fermín festival, there is a bull-run ("encierro") every morning through the streets of Pamplona.

Significance Statement

A topic of special interest in crowd dynamics, that can lead to better infrastructure management, is the study of people under high competitiveness. Persons fleeing from real danger is one instance of this scenario, but of course it is difficult to analyze it experimentally. This is why people running with bulls at the San Fermín festival provides an exceptional annual event where real data of pedestrian dynamics under extreme conditions can be collected. This kind of data is scarce and therefore highly valuable.

D.R.P., A.G., and L.A.P. designed video acquisition system; D.R.P. recorded videos; A.G.S. and J.R.C. developed tracking software; D.R.P., A.G.S., and J.R.C. processed images; D.R.P. and I.Z. analyzed data; D.R.P., A.G., L.A.P., and I.Z. wrote the paper; and D.R.P. made simulations

[1] Daniel R. Parisi. E-mail: dparisiitba.edu.ar

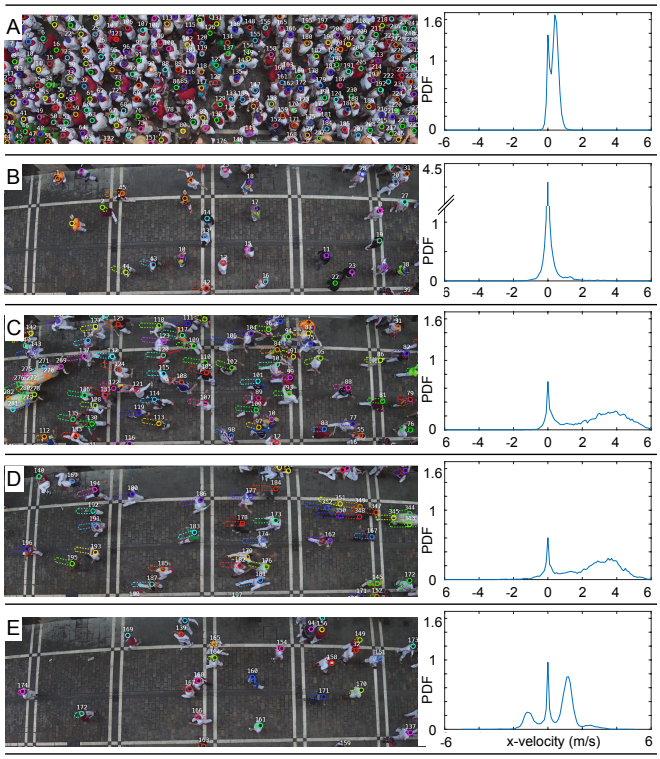

Fig. 2. States of the pedestrian system. A: state S_A, B: state S_B, C: state S_C, D: state S_D, E: state S_E. See text for description of the states. In the snapshots, labels indicate the pedestrian number, the circles mark the actual position of runners, and the dotted lines show the distance traveled by runners in a time lapse of 0.13 s (see Materials and Methods). Bulls are indicated by 6 runner-equivalent circles. On the right, the PDF of the x-component of the velocity is displayed for each state.

The course is 875-meter long, starting in a yard, and finishing in the bullring (see map in (23)). There, people run in front of six fighting bulls which are accompanied by six tamed bell-oxen. Although the distance is not too long, it is impossible for a runner to cover the whole course for several reasons, such as the presence of other runners and, above all, the high speed of the bulls (the mean speed of the bulls, in our measurement areas, is 6 m/s).

We recorded two of these runs on consecutive days (July 8 and 9, 2019) at two different locations in Estafeta street. This 300 meters long street is the most famous in the bull-run and is characterized by being relatively narrow (around 7 m wide). It starts at a corner; we have taken one recording ten meters after it, and another one at about the middle of the street length. Both locations and the corresponding field of view (FOV) are shown in Fig. 1.

Trajectories of individual bulls and runners were extracted from videos (see Materials and Methods). Bulls were marked as 6 human-equivalent positions (the mass of a bull is similar to the mass of 6 runners): one on the head, one on the beginning of the tail, and the rest on top of each leg (two over the scapulae and two over the hips). These six points were taken as 6 virtual humans when calculating the densities of neighbor runners, but were not considered in any other calculation performed in this work. The computed speeds, densities, and other related quantities, all correspond only to the runners.

In order to understand the results, it is important to know the proceedings of the festival. People are admitted into the premises at 7:15 a.m., and they wait there for 45 minutes. We have called this state S_A, in which runners first remain in place, at high density, and then walk slowly (see the x-velocity distributions, v_x, in Fig.2A and Appendix SI, Movie S1). At 8:00 a.m. the bullring door –at the end of the course– is open, and a sizable portion of the people walk into it, so that only some runners remain in the path waiting for the bulls. The street becomes less congested and, occasionally, runners are seen to warm up (Fig.2B, system state S_B). Then, a few seconds before the bulls arrive, a shock wave of running pedestrians at high velocity is observed. This shockwave triggers the starting of the race of the waiting runners. This behavior nicely correlates with the velocity distributions displayed in Fig. 2C, which show two clear peaks at $v_x = 0$ and $v_x \approx 3.5$ m/s, corresponding to what we have called state S_C. Once the bulls along with the runners in front of them have passed by, a wake of runners with decreasing speed is observed (Fig. 2D, state S_D). In about 40 or 50 seconds the system relaxes towards a situation of normal walking on a pedestrian street, eventually perturbed by lonely runners jogging at medium speed (Fig. 2E, state S_E). In summary, depending on the instant of the race, the PDF of the x-velocity displays peaks of different widths at four distinct positions corresponding to groups of people with different desired speeds, which is relevant for the forthcoming analysis. Finally, two minutes after the beginning of the race, four extra tamed bell-oxen run along the path with the purpose of guiding a possible delayed bull to the bullring.

Results

Time evolution of macroscopic observables. We start by analysing several macroscopic quantities averaged over all the $n_j(t)$ pedestrians present in each time frame (t). In particular, we calculate the mean speed $< v > (t) = \frac{\sum_{j=1}^{n_j(t)} v_j(t)}{n_j(t)}$, the mean density $< \rho > (t) = \frac{\sum_{j=1}^{n_j(t)} \rho_j(t)}{n_j(t)}$ and the mean pedestrian pressure $< P > (t) = \frac{\sum_{j=1}^{n_j(t)} P_j(t)}{n_j(t)}$. Inspired in (8, 22), P_j is the local crowd pressure $P_j = \rho_j \mathrm{Var}(v_j, knn)$ computed with the variance of the velocity over the $k = 5$ nearest neighbors for each pedestrian j (which are the same used to calculate the individual densities as explained in Materials and Methods). In Fig. 3 we display the time evolution of these variables only for the region just after the corner (similar results are obtained at the middle of the straight street). Interestingly, all quantities present a remarkable growth when the first bull enters in the field of view (defined as $t = 0$) followed by a relaxation that is rather quick for density and pressure. The relaxation seems to be slower for the case of velocity: even well after the passage of the last bull of the first group (second vertical dashed line) it seems that there is a wake of people running quite fast following the bulls toward the bullring. The passage of the later four tamed bell-oxen (second pair of vertical dashed lines) also displays a small growth of the velocity and pressure values. The low densities at which this last event occurs evidences that it is not appealing to runners. The values reported in Fig. 3B clearly correlate with the occurrence of the four last states described in Fig. 2 (S_B to S_E). State S_A (corresponding to normal walking and people waiting) took place several minutes before and is not

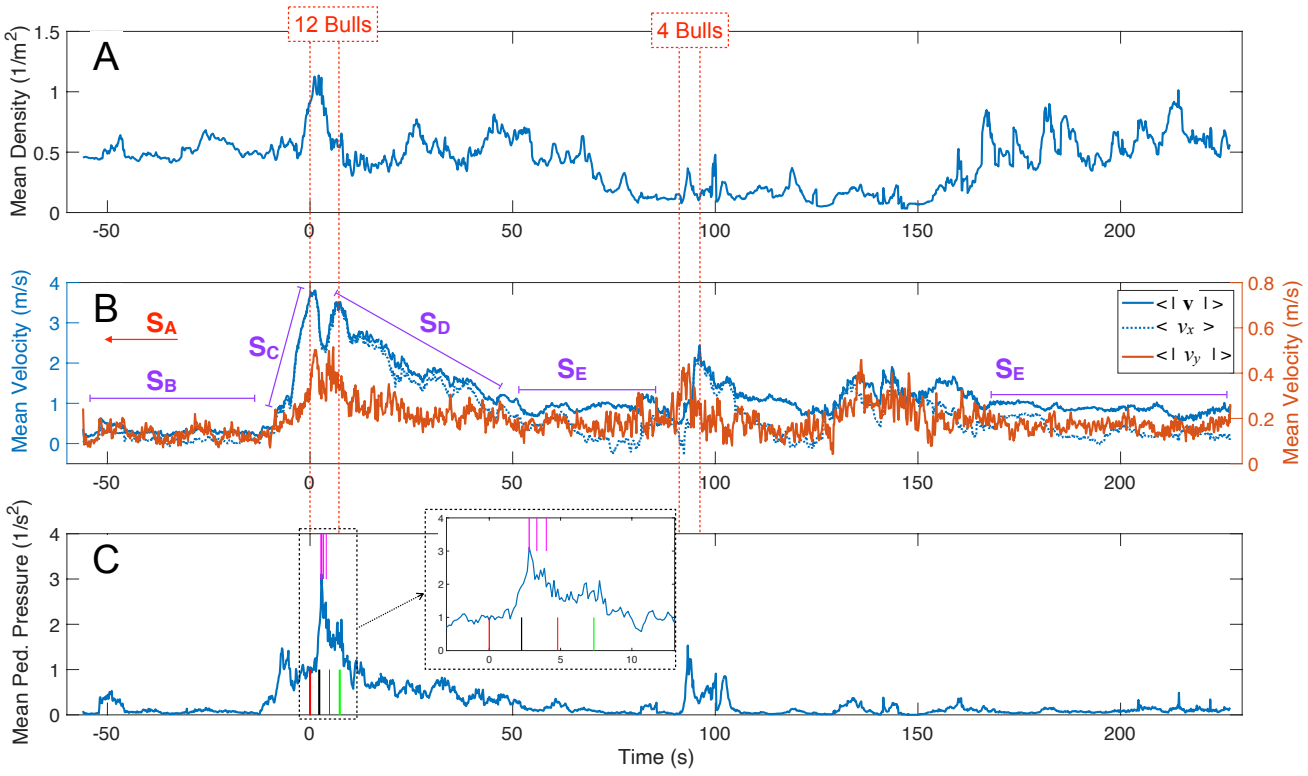

Fig. 3. Time series measured in the region after the corner. A: Mean density; B: Mean velocities (v,v_x,$|v_y|$). The states of the system S_B to S_E identified in Fig.2 are indicated in purple. The two pairs of vertical red lines indicate the passage of the first 12 bulls and the later 4 tamed bell-oxen. C: Mean pedestrian pressure. Events of falling runners are indicated with vertical color lines, the same color indicates correlated fallings. The inset corresponds to the passage of the bulls and the 2 seconds before it.

included in these time series. The mean of the absolute value of the y-component of the velocity displayed in Fig. 3B, which captures the occurrence of lateral movements, also presents a maximum when the bulls pass through the analyzed region. This feature correlates with a well known runner strategy that consists on stepping aside when they are not able to keep up the bulls pace.

Beyond all the features described above, the most striking behavior of the bull-run in the context of pedestrian dynamics is that the speed and density increase simultaneously, in clear contrast with the traditional fundamental diagrams reported in the literature. Therefore, we further look into this phenomenon by representing the speed-density relation of the averaged observables (Fig. 4), keeping the time information in the color code of the curve. Measurements at both locations along the street reveal similar behaviors. The initial state (S_B) can be identified at the beginning as a dark blue curve in the density range $\rho \in (0.4, 0.6)$ m^{-2} and mean speed around $< v > \sim 0.3$ m/s. As explained, this corresponds to runners waiting for the bulls at a fixed positions and occasionally jogging toward another location. As bulls come closer (state S_C), the mean speed increases up to a maximum (around 4 m/s) at which the density also reaches its highest value (around 1 pedestrian per square meter). After this, the system relaxes towards a normal walking situation with mean speed around $< v > \sim 1$ m/s, perturbed only when the second 4-bull pack passes displaying a velocity peak at lower densities. We emphasize that only pedestrian data were used for computing these quantities.

Despite the complicated dynamics, if we look only at the speed-density relation, it is evident that the general rule of decreasing speed when the pedestrian density increases, is not fulfilled. Noteworthy, a monotonically decreasing speed-density relation has been consistently observed in dozens of different scenarios, including competitive situations (8, 22). Therefore, as far as we know, this is the first speed-density relation that seems to deviate from the general rule. Of course, several differences can be outlined between the bull-run, and most pedestrian systems. The first one is that in this case, the process is non-stationary as the irruption of bulls introduces a big perturbation in the system. Another one concerns the willingness of pedestrians to run in front of the bulls. Finally, it should be also noted that, if we consider the whole process, a wide range of desired velocities are present in the system. Therefore, in the following section, we investigate this problem by analysing the speed-density relation from a microscopic point of view.

Untangling the San Fermín speed-density relation. In Fig. 5A, we represent with gray dots the values of velocity versus density, as calculated at the individual runner level (see Materials and methods) in all the frames registered at both street locations, as indicated in Fig. 1, and including those in the state S_A (which were not present in the time series). Contrary to the observation made in the mean speed-density diagram for states S_B to S_E (Fig. 4), when including state S_A the data cloud seems to suggest a reduction of the velocity as the density increases. Also, it is interesting to note that the points cluster in two overlapping but well differentiated groups: one for

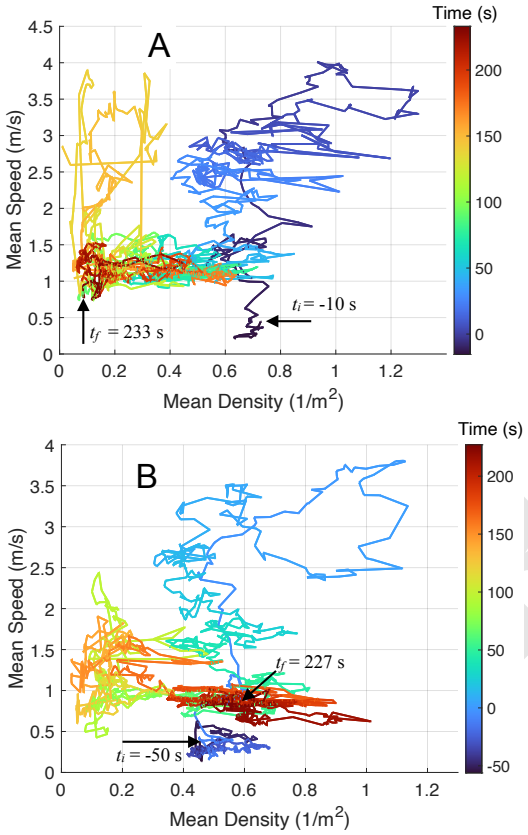

Fig. 4. Mean speed-density diagram. A: In the middle of the straight street. B: In the region "after the corner". The time evolution is encoded by colors as indicated in the colorbars.

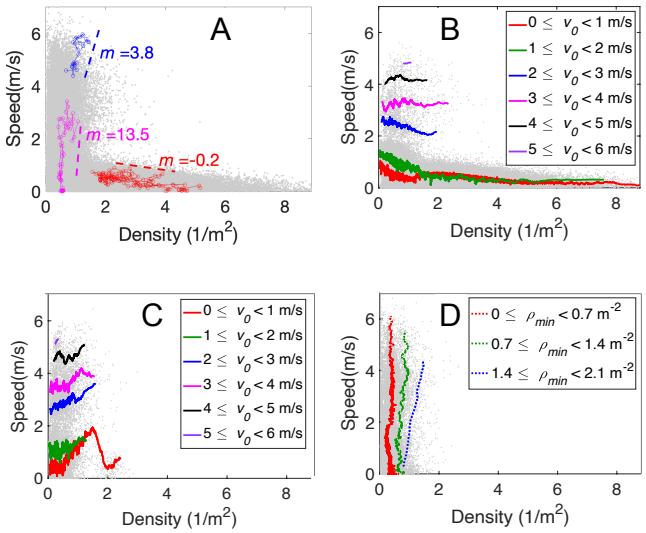

Fig. 5. Microscopic speed-density data points. A: Gray dots represent all pedestrian data obtained from the whole race for the two recorded locations. Solid colors, three examples of individual pedestrian trajectories in the speed-density space. The dashed lines and the m value in their corresponding color display the slope of the principal component vector for each trajectory. B: Speed-density data for pedestrian showing normal behavior (i.e. $m \in [-1, 0]$) and the corresponding speed-density curves obtained by computing the moving average of the data when grouped according to its speed at minimum density as indicated in the legend. C: Speed-density data for pedestrian showing atypical behavior (i.e. $m \in [1, 10]$) and the corresponding speed-density curves obtained as moving average the data, when classified according to its speed at minimum density as indicated in the legend. D: Speed-density data for pedestrian showing extreme behavior (i.e. $|m| > 10$) and the corresponding speed-density curves obtained by performing a moving average of the data when classified according to its density at minimum velocity as indicated in the legend.

low densities ($\rho < 2$ m^{-2}) where the velocities span from 0 to 7 m/s that, in Fig. 5A, appears as a vertical cloud of points; and the other for high densities ($\rho > 2$ m^{-2}) where the velocities are always smaller than 1.5 m/s and in Fig. 5A appears as a cloud of points with an envelope that has a slightly decreasing slope. There is a depleted region in the speed-density plane: runners struggle to reach velocities above 1.5 m/s when $\rho > 2$ m^{-2}. Interestingly, within all the data points represented in Fig. 5A, we can distinguish very different pedestrian behaviors depending on the runner analyzed and the specific state of the race as described above. As an example, in Fig. 5A we show three characteristic trajectories in the speed-density space (each corresponds to a different pedestrian). Among the trajectories, we can distinguish a "standard" one occurring at high densities in which the speed reduces as the density increases. Nevertheless, there are other (less common) trajectories where we observe a wide range of speed values for the same or similar (low) densities. This behavior is a piece of clear evidence that pedestrians may change their desired speed with time. For example, pedestrians waiting for the bulls have zero desired speed and, as the bulls come closer, they begin to run rising the desired speed up to the maximum.

To classify the different behaviors, we perform a principal component analysis (PCA) for each trajectory in the speed-density space and use the slope (m) of the first direction vector as a classification parameter. This direction is the one that maximizes the variance of the data (24). Examples of these vectors are shown in Fig. 5A as dashed lines along with their

slope values. Then, we choose three groups of pedestrians: (1) pedestrians with $m \in [-1, 0]$ are said to display "*normal behavior*" since the speed decreases when the density grows; (2) pedestrians showing $m \in [1, 10]$ are considered to be in an "*atypical*" scenario because the speed increases with increasing density; (3) finally, when $|m| > 10$ we have pedestrians in an "*extreme condition*" as there is an important variation of speed for a rather constant density value.

Next, in Figs. 5B,C,D, we represent the data points of the speed-density relation that correspond to each class (normal, atypical and extreme, respectively). Figure 5B reveals that almost all data in the speed-density relation for which $\rho > 2$ m^{-2} correspond to pedestrians displaying normal behavior. On the contrary, a small portion of the data obtained for small values of ρ corresponds to this class of motion. Considering only pedestrians displaying normal behavior, we group individual trajectories according to the speed v_0 at their minimum density (this can be seen as an approximation of the free speed for each given trajectory). Then, we implement a moving average of the data corresponding to each subgroup obtaining the results represented in the same Fig. 5B. In most cases, the relation is consistent with the traditional negative slope encountered in the literature. However, as the free speed values increase, it is more likely to find almost horizontal curves indicating a constant speed independent of the density. It is reasonable to think that for high competitiveness, as the moving threat approaches, runners want to maintain the maximum speed no matter the density. Also, it is interesting to note that the curves corresponding to $0 \leq v_0 \leq 1$ m/s and $1 \leq v_0 \leq 2$ m/s are clearly distinguishable when the density is smaller than 2 m^{-2}, but coincide for higher densities. This feature -already reported for pedestrian dynamics (7, 16), and in a system involving cars and lorries (25)- suggests that the desired speed has a crucial role in the dynamics observed in dilute conditions, but it becomes less relevant as the density increases. Although our data at high density correspond to state S_A (people with slow desired velocity), in other systems the zone of high density and low speed could display a particular regime of people pushing each other that can cause instabilities, as observed in experiments (22, 26) and turbulent flows as reported for crowd catastrophes (8, 27).

In Fig. 5C we show a similar analysis to the one implemented for normal conditions, but for the atypical condition. In this case, the cloud of gray dots shows that the atypical behavior always corresponds to situations of low density ($\rho < 2$ m^{-2}). Again, if we group runners according to their speeds v_0 at minimum density, we observe a consistent set of features for instance, that the curves display positive slopes and the separation between them (with the only exception of the two obtained for the smallest values of v_0). All these characteristics, together with the weak dependence of the speed on the density observed for low density values and high desired speeds shown in Fig. 5B, strongly suggest that the only parameter governing the runners behavior in dilute conditions is their desired speed.

Finally, the extreme scenario of pedestrians displaying $|m| > 10$ are, as expected, observed in the region of $\rho < 2$ m^{-2} (Fig. 5D). In this case, as trajectories are almost vertical, the moving average is computed along the speed axes, grouping trajectories depending on the value of their minimum density. As in the atypical scenario described above, the observed behavior would correspond to pedestrians changing their desired speed for near-constant density values. Nevertheless, the fact that the slopes in the speed-density relation reduce as the initial density augments, suggests that pedestrians ability to reach very high velocities diminishes as the density grows. Indeed, this result supports the previously mentioned idea of the existence of a inaccessible region in the speed-density diagram (speeds above 1.5 m/s and $\rho > 2$ m^{-2}).

The inaccessible region in the speed-density relation. In this section we delve into the existence of the inaccessible region of the speed-density space. The question is whether the absence of data for speeds above 1.5 m/s and $\rho > 2$ m^{-2} has a psychological reason (i.e. people voluntarily decide to avoid running at high densities); or else, if there is any physical constraint that prevents the entry into this area of the parameter space. In order to shed light on this we have carefully analyzed the falls of the runners, because we have realized that a remarkable proportion of these incidents coincide with the passage of the bulls (which is the situation of higher speed and density).

Indeed, the events with multiple falling people have paramount importance because they can trigger massive pile-ups that may cause a large amount of casualties. Several falls involving a large number of persons have occurred in previous years, mainly at the narrowest part of the path (the entrance of the bullring), as in 1957 (28) and 1977 (29), or more recently in 2013 (30). Although these big pile-ups are sporadic, single falls or small-group falls are more frequent, and some instances were seen in our recordings. In particular, we observed a total of 20 people falling, 13 on the first day, and 7 on the second day. All of them took place during the passage of the bulls, coinciding with a scenario of high average density, velocity and crowd pressure, as shown with vertical colored lines in Fig. 3C for day 2 (the same occurs for day 1). This seems a piece of new evidence in favor of the hypothesis of Helbing et al (8) who proposed that the crowd pressure can be correlated with the probability of falling.

Indeed, it is natural to assume that the first falling and the consecutive ones will occur with increasing probability when augmenting both, the crowd speed variance and density. Less available space can cause accidental physical contact of runners, which may affect their motion and trigger their falling. Therefore, the probability of falling in the bull-run will vary drastically over time, being only significant in the transition between states S_C and S_D coinciding with the bulls passage. But not only this, also the falling probability will also depend on, for example, the occurrence of a previous fall, i.e. the presence of a runner on the floor. Indeed, it is interesting to note that only 6 falls were independent (uncorrelated) whereas 14 of them belonged to a small-group fall. Although our sample size is small, we estimate a falling probability by counting the ratio between the number of falls and the number of runners between the first and last of the 12-pack bulls. If we include runners from the frame in which the head of the first bull exits the FOV to the frame when the tail of the last bull enters the FOV, we counted 97 runners (both days combined). Thus, the 20 observed falls lead to a falling probability of about 0.21. Note that this value might be likely an overestimation. If we consider instead the interval between the entrance of the first bull in the FOV to the exit of the last one, the fall probability would be 0.08. The data presented in Fig. 6 (blue) corresponds to this last computation.

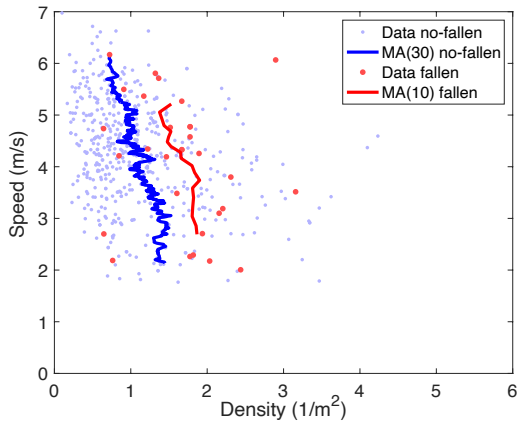

Fig. 6. Microscopic speed-density data for pedestrians identified at the time of the bulls passage. For each pedestrian, two points are represented, one for his/her maximum velocity and another for his/her maximum local density. Red and blue dots represent data for pedestrians that fall and do not fall, respectively, as indicated in the legend. In the case of falling, the data belongs to the trajectories before the falling event. Red and blue solid lines represent the moving averages along the speed axis computed for each case.

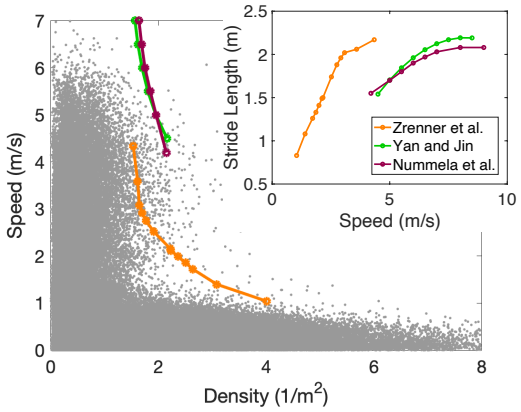

Fig. 7. Theoretical limit in the speed-density diagram given by the bio-mechanical data of the stride length of runners required for a given speed (see text). Reported data correspond to Zrenner et al. (31), Nummela et al. (32) and, Yan and Jin (33).

In order to decide if there is any relationship between the falling events and the inaccessible region in the speed-density diagram, in Fig. 6 we compare the microscopic speed-density relations for the falling pedestrians with the non-falling pedestrians. For this comparison, only the data of non-falling pedestrians that are in the videos during the falling events (i.e. when the bulls cross through the field of view) are considered. In addition, given that falling events are probably related with extreme values of either speed or density, we only draw in the plot two points for each runner: one represents the pedestrian velocity when the density at the pedestrian location is maximum; the other, the density at the pedestrian location corresponding to the maximum velocity of that particular pedestrian. Then, we compute the moving averages of each group of data separately (taking the speed axis as the independent variable), evidencing a clear shift towards higher densities for the case of pedestrians that fall. We propose that the moving average line corresponding to falling pedestrians could be seen as a boundary separating zones of physically allowed speed-densities from another zone in which the pedestrian system would collapse because of the occurrence of falls. Indeed, this hypothesis is supported by the fact that the position of this vertical line seems to coincide with the density and velocity values above which the density of points in the global microscopic speed-density relation is dramatically reduced (Fig. 5A).

Another strong argument for the existence of an inaccessible region in the speed-density diagram can be put forward from independent bio-mechanical arguments if we consider that the higher the runner speed, the more available space is needed to take a step. Indeed, the relation between the runners speed and their stride length (L_S) has been reported in Ref. (31–33). These studies show that the stride length increases with speed as shown in the inset of Fig. 7. The maximum local density ρ_i at which a pedestrian can make a stride L_S can be estimated as $\rho_i = 1/(L_S\ W_e)$, with W_e the effective runner width (see SI Appendix, Fig. S1). Then, using Ref. (31–33), we can obtain the minimum space (maximum density) required by runners to take a step depending on their speed (see solid lines in Fig. 7). In other words, these curves separate physically accessible from inaccessible regions in the speed-density diagram. Interestingly, the theoretical limit obtained is close to the empirical boundary marking the zone of the diagram where runners are at a high risk of falling, as shown in Fig. 6.

Encompassing macroscopic and microscopic behavior. After having identified the different type of individual behaviors leading to the microscopic speed-density diagram shown in Fig. 5, we are in a position to explain the origin of the counterintuitive macroscopic speed-density plots displayed in Fig. 4. To this end, knowing the type of individual behavior predominating at each moment becomes crucial. For this reason, in SI Appendix, Fig. S2, we report the temporal evolution of the number of pedestrians that belong to the three different types of behavior (normal, atypical and extreme) together with the different stages of the race depicted in Fig. 2. We further filter these signals considering normal behavior only for pedestrians with $v < 1.7$ m/s and $v > 1.7$ m/s in the other two cases. Clearly, before the approach of the bulls (stage S_B) pedestrians behave normally ($m \in [-1, 0]$), a pattern that is dramatically altered when the animals arrive to the field of view. At this moment (stage S_C), the number of pedestrians behaving normally goes to zero and there is a peak of people showing atypical and extreme behavior. During the next 50 seconds or so (stage S_D), there is a gradual relaxation of the number of atypical and extreme runners accompanied by a growth in the number of normal pedestrians. After about 50 seconds (stage S_E), the main observed behavior is the normal one, maybe with a small alteration at approximately 100 seconds, when the second pack of tamed bell-oxen passes through the analyzed region. Note also that, for the high density and non-competitive condition of the stage S_A (not shown in the graph as it occurs long before the arrival of the bulls), all the individual data fall in the region corresponding to normal condition where the speed reduces with the density for $\rho > 2$ m^{-2} (inset of SI Appendix, Fig. S2).

Overall, we observe normal behavior (i.e. $m \in [-1, 0]$) in most situations with the exception of the time at which the bulls arrive and the 40-50 seconds thereafter. At these stages, the runners display either atypical behavior or extreme

one, coinciding with the positive correlation of the average velocity and the macroscopic density shown in Fig. 4. If we consider the presence of the bulls as a perturbation similar to the one studied by Nicolas et al. (34), the runners clearly anticipate it and start running. Moreover, the fact that the bulls occupy a big fraction of the available area of the street and the willingness of runners to approach the bulls, causes a sudden increase in the density. In this sense, we can state that both, pedestrian interactions and the special nature of the perturbation triggering their motion, determine the observed dynamics.

Discussion

In this work, we have shown that the speed-density relation in the San Fermín festival does not correspond to any of the fundamental diagrams reported so far for pedestrians in normal or competitive conditions. Indeed, the increase of the average velocity with the systems' average density is at odds with established rules on pedestrian dynamics. Apart from the fact that the running of the bulls is a time-dependent process, we have revealed that the key aspect behind this unusual feature is the variety of ways in which people behave.

Based on the results in the previous sections, we put forward the following explanation for the observed "bull-run" fundamental diagram:

- Instead of a single speed-density relation, there exist many curves which correspond to a broad range of desired speeds. Indeed, as the desired speed grows the curves become flatter for a range of small densities (Fig. 5B). This can be explained if one assumes that runners that are at maximum risk have a very high desired speed no matter the density.
- The counterintuitive behavior of increasing speed with increasing density would reflect pedestrians changing between different curves corresponding to different desired speeds. It shows that an important number of pedestrians wait for the arrival of the bulls and, at that moment they increase their desired speed, leading to a behavior as the one shown in Fig. 5C and D.
- For very fast runners, high local densities increase the danger of falls, a feature that can be rationalized in terms of the stride length dependence on the speed. Therefore, it is reasonable to assume that a physical boundary exists for high speeds and high densities. The red line in Fig.6 and curves on Fig.7 can give a qualitative idea of the position of this boundary in the speed-density diagram.

In Fig. 8A we sketch the different speed-density relations that have been identified. The curves represent particular cases of the Kladek-Newell-Weidmann formula (1, 3, 35), an analytical expression having the flexibility to fit observed speed-density diagrams (see Materials and methods). Note that our proposal suggests that the curves corresponding to the highest desired velocities drop to a speed equal to zero for high densities, illustrating the collapse of the system that can be expected when runners try to run too fast at such crowded conditions. Moreover, the curve for $v_0 = 7$ m/s represents a part of the boundary between accessible and inaccessible areas in the speed-density diagram. The lower v_0 curves try to reproduce the experimental ones shown in Fig.5B. The curve for $v_0 = 2$ m/s represents an enveloping curve of the data points displayed as a gray cloud in Fig.5A and Fig.7. Also, it

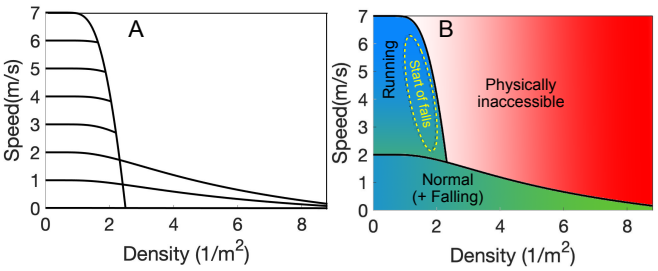

Fig. 8. Hypothetical high-speed fundamental diagram. A: Possible speed-density curves for different desired speeds $v_0 = v(\rho = 0)$ (see eq.2). B: Proposed state diagram with, at least, three different regimes.

marks the lower boundary of the accessible-inaccessible limit, coinciding with the curve of Zrenner et al. in Fig.7. The limit $v_0 = 0$ m/s means that if all pedestrians had zero desired speed, the crowd would not move no matter the density.

Regardless of the particular shape of the curves for the various desired speeds, the combination of them will lead to a generalized speed-density space similar to the one sketched in Fig. 8B. In there, different regions can be distinguished: (i) a fleeing region for low densities in which pedestrians would be able to change their desired velocity and jump between different curves; (ii) a inaccessible region for high velocities and densities at which pedestrians would have a high probability of falling; and (iii) a normal region for pedestrians with low desired speeds where the speed reduces with increasing density as usually observed in steady state crowds. Note that in this region walking pedestrians coexist with those that wanted to run but suffer a fall. This degeneration could be broken if we include the desired speed as a third state variable, which in the case of a falling pedestrian, can be approximated by the actual speed at which the falling begins.

In order to test the above explanation of the peculiar speed-density relation observed in Fig. 4, we carried out simulations for states S_C and S_D. To this end, we used the contractile particle model (36), which has been shown to reproduce the experimental speed-density data for pedestrian systems under normal conditions. Except for the constant desired velocities, all the other parameters of the model are set in the range of those reported in Ref. (36). For a description of this model along with its parameters see the SI Appendix.

The main new aspect that we introduce in the simulations is the time-dependent nature of the desired velocities, which depend on the distance to the bulls. The simulation area has 6 m in width and 18 m in length (see Appendix SI, Fig. S3). Initially, a set of $n_0 = 40$ waiting agents are distributed uniformly within this area with desired speed $v_0 = 0$ m/s. Three seconds after the simulation starts, a pack of 10 bulls enters the simulation area at a fixed speed $v_b = 6$ m/s. Around the bull pack, a new group of $n_1 = 20$ agents enter the simulation area (this kind of increase in the number of runners was observed in our data, see Appendix SI, Fig. S4, and Movies S2 and S3) and its desired velocities are in the range $v_0 \in (4.8, 6)$ m/s. Each of the n_0 waiting particles activate (i.e., switch its own v_0 to a positive value) when the first bull particle is at a distance (in the x-direction) of 9 m from its position. At that moment, the desired speed of the waiting particle changes to a random value $v_0 \in (4.8, 7.2)$ m/s. Agents behind the bulls

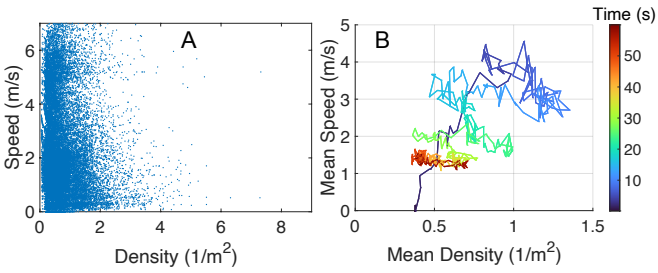

Fig. 9. Simulation results of states S_C and S_D. A: Individual speed-density data. B: Average speed and density in each time frame. The time evolution is encoded in color.

slow down changing the desired speed linearly with time until it reaches a walking value in the range $v_0 \in (0.75, 2.25)$ m/s at about 40 s since the simulation started.

The results of the simulations shown in Fig.9 reproduce the same kind of dynamics as observed in the real system. Figure 9A displays microscopic information of local density and speed. If we compared this cloud of point with the one in Fig.7 (or Fig.5A) we can observe the equivalent vertical development of the data at low-density corresponding to the change of the desired velocities with time. In Fig. 9B, the time evolution of the mean speed and density qualitatively matches the results observed in the San Fermín system displayed in Fig. 4 in which the mean speed and density increase simultaneously. It should be noted that the simple model used, does not consider either falls, or avoidance mechanisms. However, the inaccessible region of the speed-density diagram is apparent.

In summary, after recording and analysing a real and emblematic pedestrian system in which people display several states of behavior including high-speed fleeing from a moving threat, we observed for the first time a positive correlation between speed and density which can be explained in terms of time-dependent desired speed, which is determined by the bulls presence. Furthermore, using this new information we postulate a generalization of the traditional fundamental diagram of pedestrian dynamics that encompasses the different behaviors observed.

Materials and methods

Image acquisition and processing. The video camera used was a FLIR DUO PRO R 640 45°FOV and it was placed at approximately 15 m over the street floor. Visible and infrared images were taken, but we only used the visible channel that has a resolution of 3840 x 2160 pixels and a frame rate of 30 fps (time interval $dt = 1/30$ s). Each image was reduced to 960 x 540 pixels and further cropped in order to cut-off walls and buildings from the image, leaving a final useful image with bulls and pedestrians of about 960 x 350 pixels. Also the time resolution was reduced to $dt = 4/30$ s $= 0.13$ s when analyzing the images.

The images were processed semi-automatically. For this, we developed an *ad-hoc* software that allows the users to label in subsequent frames each pedestrian head by clicking with the computer mouse on the image and correct it if necessary. The software can go forward and backward along the recording taking one frame out of every four, effectively reducing the frame rate to $dt = 4/30$ s. The main source of error in the pedestrian location is the size of their heads and the height of people. We estimated that this error was about 0.15 m, that is reduced to about 0.12 m with smoothing (see below). Once the positions of all runners and bulls were obtained, they were corrected for the lens distortion using the function "undistortPoints" of OpenCV library (37). We assumed no tangential distortion on the lens and determined the quadratic radial distortion coefficient empirically, using as reference known straight lines in the picture.

Finally, in order to reduce acquisition fluctuations, each trajectory $x_i'(t)$ and $y_i'(t)$ are smoothed by interpolating them with a generalized regression neural network (GRNN) (38) with spread value $\sigma = 1$.

It must be noted that because of the zenithal camera position, the distance to the people, and the resolution used, the actual identity of each runner is preserved. The "Comité de Ética de la Investigación de la Universidad de Navarra" (Research Ethics Committee of the University of Navarra) has assessed this manuscript and has found no ethical objections.

Microscopic Velocity and Density Calculation. From the $x_i(t)$, $y_i(t)$ positions, the velocities were computed as $v_{xi}(t) = \frac{x_i(t) - x_i(t-0.13\ \mathrm{s})}{0.13\ \mathrm{s}}$ and $v_{yi}(t) = \frac{y_i(t) - y_i(t-0.13\ \mathrm{s})}{0.13\ \mathrm{s}}$, and the speed as $v(t) = \sqrt{v_x^2(t) + v_y^2(t)}$.

The local density is calculated by means of the non-parametric k-nearest neighbors (k-nn) method already considered for similar systems (39, 40). This method allows computation of the density at any arbitrary point (x, y) in the space. It relies on measuring the distance to the k^{th} nearest neighbor (d_k) of the point (x, y). In our case, we choose the points in space coinciding with each runner i, in consequence, the first neighbor of the space point (x, y) is (x_i, y_i) being at zero distance. Then, the density is computed as $\rho_i = \frac{k-1}{\pi\ d_k^2}$ (see SI Appendix, Fig. S5). We took $k = 5$. If the circle of radius d_k lies out of the boundary, a correction is made by subtracting the portion of the circle area A_{OUT} lying outside the image (see SI Appendix, Fig. S5), so the density reads:

$$\rho_i = \frac{k-1}{\pi\ d_k^2 - A_{OUT}}. \qquad [1]$$

It must be noted that this definition also works when one or more of the k-nn points correspond to a bull.

We compare this method for calculating local densities with another considering the Voronoi area for each particle (41) and, for $k = 5$, the differences between the two methods are less than 0.35 %.

Kladek-Newell-Weidmann Pedestrian Fundamental Diagram. The curves of the generalized pedestrian fundamental diagram of Fig. 8 have the functional form of the Kladek-Newell-Weidmann formula, as stated in Ref. (1, 3, 35).

$$v(\rho) = v_0(1 - e^{-g(\frac{1}{\rho} - \frac{1}{\rho_{max}})}), \qquad [2]$$

where g and ρ_{max} are constants; in particular, ρ_{max} is the density at which the speed drops to zero. The particular values used for curves in Fig. 8 are shown in SI Appendix, Table S1.

Data Availability. All study data are included in the article and/or SI Appendix.

ACKNOWLEDGMENTS. We acknowledge financial support from grants ITBACyT 2018-42 (Instituto Tecnológico de Buenos Aires),

PID 2015-003 (Agencia Nacional de Promoción Científica y Tecnológica, Argentina), HFSP Research Grant (Ref.-No: RGP0053/2020) and from Spanish Government through Project FIS2017-84631-P, MINECO/AEI/FEDER, UE. We are also grateful to Lucas S. Gómez, Tamara Puig, Julian F. Arce Doncella and Esteban Capolicchio for their assistance with the semi automatic image processing. DRP thanks Hernán J. Gómez and Gracián Garcés Díaz for their help in the recording of videos.

1. Tobias Kretz. An overview of fundamental diagrams of pedestrian dynamics. https://www.researchgate.net/profile/Tobias-Kretz-2/publication/336286296_An_overview_of_fundamental_diagrams_of_pedestrian_dynamics/links/5d99ea63458515c1d39abe71/An-overview-of-fundamental-diagrams-of-pedestrian-dynamics.pdf, 2019. [Online; accessed 22-April-2021].
2. Rafegh Aghamohammadi and Jorge A Laval. Dynamic traffic assignment using the macroscopic fundamental diagram: A review of vehicular and pedestrian flow models. *Transportation Research Part B: Methodological*, 2018.
3. Ernst Bosina. *A New Generic Approach to the Pedestrian Fundamental Diagram*, volume 183. ETH Zurich, 2018.
4. Rainald Lohner, Britto Muhamad, Prabhu Dambalmath, and Eberhard Haug. Fundamental diagrams for specific very high density crowds. *Collective Dynamics*, 2:1–15, 2018.
5. Jun Zhang. *Pedestrian fundamental diagrams: Comparative analysis of experiments in different geometries*, volume 14. Forschungszentrum Jülich, 2012.
6. Cheng-Jie Jin, Rui Jiang, SC Wong, Dawei Li, Ning Guo, and Wei Wang. Large-scale pedestrian flow experiments under high-density conditions. *arXiv preprint arXiv:1710.10263*, 2017.
7. Anders Johansson. Constant-net-time headway as a key mechanism behind pedestrian flow dynamics. *Physical review E*, 80(2):026120, 2009.
8. Dirk Helbing, Anders Johansson, and Habib Zein Al-Abideen. Dynamics of crowd disasters: An empirical study. *Physical review E*, 75(4):046109, 2007.
9. Armin Seyfried, Bernhard Steffen, and Thomas Lippert. Basics of modelling the pedestrian flow. *Physica A: Statistical Mechanics and its Applications*, 368(1):232–238, 2006.
10. Armin Seyfried, Bernhard Steffen, Wolfram Klingsch, and Maik Boltes. The fundamental diagram of pedestrian movement revisited. *Journal of Statistical Mechanics: Theory and Experiment*, 2005(10):P10002, 2005.
11. Ulrich Weidmann. Transporttechnik der fußgänger: transporttechnische eigenschaften des fußgängerverkehrs, literaturauswertung. *IVT Schriftenreihe*, 90, 1993.
12. Masamitsu Mōri and Hiroshi Tsukaguchi. A new method for evaluation of level of service in pedestrian facilities. *Transportation Research Part A: General*, 21(3):223–234, 1987.
13. Francis P Navin and Robert J Wheeler. Pedestrian flow characteristics. *Traffic Engineering, Inst Traffic Engr*, 39, 1969.
14. SJ Older. Movement of pedestrians on footways in shopping streets. *Traffic engineering & control*, 10(4), 1968.
15. BD Hankin and Richard A Wright. Passenger flow in subways. *Journal of the Operational Research Society*, 9(2):81–88, 1958.
16. Xiangxia Ren, Jun Zhang, and Weiguo Song. Flows of walking and running pedestrians in a corridor through exits of different widths. *Safety Science*, 133:105040, 2021.
17. John J Fruin. Pedestrian planning and design. Technical report, 1971.
18. Vitaly M Predtechenskii and Anatolii Ivanovich Milinskii. *Planning for foot traffic flow in buildings*. National Bureau of Standards, US Department of Commerce, and the National ..., 1978.
19. Philip J DiNenno. Sfpe handbook of fire protection engineering. 2008.
20. Morgan J Hurley, Daniel T Gottuk, John R Hall Jr, Kazunori Harada, Erica D Kuligowski, Milosh Puchovsky, John M Watts Jr, CHRISTOPHER J WIECZOREK, et al. *SFPE handbook of fire protection engineering*. Springer, 2015.
21. Dirk Helbing. A mathematical model for the behavior of pedestrians. *Behavioral science*, 36 (4):298–310, 1991.
22. Angel Garcimartín, José Martín Pastor, César Martín-Gómez, D Parisi, and Iker Zuriguel. Pedestrian collective motion in competitive room evacuation. *Scientific reports*, 7(1):1–9, 2017.
23. https://www.google.com/maps/d/viewer?mid=1zU4804rRF3S6z-8Hyz8Q3Q7bO-Q&ll=42.8179127889818%2C-1.6428772000000036&z=17/. [Online; accessed 20-January-2021].
24. Ian T Jolliffe. Principal components in regression analysis. In *Principal component analysis*, pages 129–155. Springer, 1986.
25. Dirk Helbing and Bernardo A Huberman. Coherent moving states in highway traffic. *Nature*, 396(6713):738–740, 1998.
26. Ángel Garcimartín, Diego Maza, José Martín Pastor, Daniel Ricardo Parisi, César Martín-Gómez, and Iker Zuriguel. Redefining the role of obstacles in pedestrian evacuation. *New Journal of Physics*, 20(12):123025, 2018.
27. Mehdi Moussaïd, Dirk Helbing, and Guy Theraulaz. How simple rules determine pedestrian behavior and crowd disasters. *Proceedings of the National Academy of Sciences*, 108(17): 6884–6888, 2011.
28. https://www.youtube.com/watch?v=4q6Z2vxIPEw/. [Online; accessed 20-Jenuary-2021].
29. https://www.youtube.com/watch?v=Jkou4uexgdI/. [Online; accessed 20-Jenuary-2021].
30. https://www.youtube.com/watch?v=ilShtXwKVFI/. [Online; accessed 20-January-2021].
31. Markus Zrenner, Stefan Gradl, Ulf Jensen, Martin Ullrich, and Bjoern M. Eskofier. Comparison of different algorithms for calculating velocity and stride length in running using inertial measurement units. *Sensors*, 18(12), 2018. ISSN 1424-8220. . URL https://www.mdpi.com/1424-8220/18/12/4194.
32. A Nummela, T Keränen, and LO Mikkelsson. Factors related to top running speed and economy. *International journal of sports medicine*, 28(08):655–661, 2007.
33. Songhua Yan and Jichun Jin. Study on stride length, rate, ans speed of 100m sprinte running with five kinds of speed. In *ISBS-Conference Proceedings Archive*, 2004.
34. Alexandre Nicolas, Marcelo Kuperman, Santiago Ibañez, Sebastián Bouzat, and Cécile Appert-Rolland. Mechanical response of dense pedestrian crowds to the crossing of intruders. *Scientific reports*, 9(1):1–10, 2019.
35. Gordon Frank Newell. Nonlinear effects in the dynamics of car following. *Operations research*, 9(2):209–229, 1961.
36. Gabriel Baglietto and Daniel R Parisi. Continuous-space automaton model for pedestrian dynamics. *Physical Review E*, 83(5):056117, 2011.
37. https://docs.opencv.org/3.4/da/d54/group__imgproc__transform.html#ga55c716492470bfe86b0ee9bf3a1f0f7e. [Online; accessed 24-July-2021].
38. Donald F Specht et al. A general regression neural network. *IEEE transactions on neural networks*, 2(6):568–576, 1991.
39. Daniel R Parisi, Didier Sornette, and Dirk Helbing. Financial price dynamics and pedestrian counterflows: A comparison of statistical stylized facts. *Physical Review E*, 87(1):012804, 2013.
40. German A. Patterson, Didier Sornette, and Daniel R Parisi. Properties of balanced flows with bottlenecks: Common stylized facts in finance and vibration-driven vehicles. *Physical Review E*, 101(4):042302, 2020.
41. Bernhard Steffen and Armin Seyfried. Methods for measuring pedestrian density, flow, speed and direction with minimal scatter. *Physica A: Statistical mechanics and its applications*, 389 (9):1902–1910, 2010.